JOURNAL OF AIRCRAFT
Vol. 42, No. 1, January–February 2005

Wind-Tunnel Interference Effects on Delta Wing Aerodynamics Computational Fluid Dynamics Investigation

M. R. Allan,* K. J. Badcock,† G. N. Barakos,‡ and B. E. Richards§
University of Glasgow, Glasgow, Scotland G12 8QQ, United Kingdom

Reynolds averaged Navier–Stokes simulations of a static and pitching delta wing within three wind tunnels have been performed. These simulations have been compared with the case of the wing in free air to ascertain the various influences of the walls on the vortical flow. The presence of tunnel walls has been found to promote vortex breakdown, with side wall proximity being the dominant factor. Roof and floor proximity has been seen to have a negligible effect on vortex breakdown. During pitching motion, side wall proximity delays vortex reformation after breakdown has reached its most upstream location, during cyclic pitching motion. This delay is recovered on the upstroke of the motion. These results confirm previous work with Euler simulations of tunnel interference.

Nomenclature

b = wing span
C_D = drag coefficient, $D/(q_\infty S)$
C_L = lift coefficient, $L/(q_\infty S)$
C_M = pitching moment coefficient, $M/(q_\infty S c_r)$
C_P = pressure coefficient, P/q_∞
c_r = root chord
D = drag
f_0 = model oscillation frequency
H = tunnel height
K = reduced frequency of pitching motion, $2\pi f_0 c_r/U_\infty$
k = kinetic energy of turbulent fluctuations per unit mass
L = lift
M = pitching moment
M_∞ = freestream Mach number
P = pressure
P_k = limited production of k
P_k^u = unlimited production of k
q_∞ = freestream dynamic pressure, $(\frac{1}{2})\rho U_\infty^2$
Re = Reynolds number, $\rho U_\infty c_r/\mu$
r = ratio of magnitude of rate of strain and vorticity tensors
S = wing area
t = time
U_∞ = freestream velocity
u_r = friction velocity
W = tunnel width
x = chordwise coordinate
y^+ = dimensionless, sublayer-scaled, distance, $u_\tau y/\nu$
α = angle of attack
α_m = mean angle of attack
α_0 = pitch oscillation amplitude
β^* = closure coefficient (0.09)
Γ = circulation
η = spanwise coordinate/local span
μ = dynamic viscosity
ν = kinematic viscosity
ρ = mass density
τ = nondimensional time, tU_∞/c_r
ϕ = helix angle
ω = specific dissipation rate

Presented as Paper 2003-4214 at the AIAA 21st Applied Aerodynamics Conference, Orlando, FL, 23–26 June 2003; received 19 September 2003; revision received 27 January 2004; accepted for publication 27 January 2004.

*Research Assistant, Department of Aerospace Engineering, Computational Fluid Dynamics Laboratory. Member AIAA.
†Reader, Department of Aerospace Engineering, Computational Fluid Dynamics Laboratory. Member AIAA.
‡Lecturer, Department of Aerospace Engineering, Computational Fluid Dynamics Laboratory. Member AIAA.
§Mechan Professor, Department of Aerospace Engineering, Computational Fluid Dynamics Laboratory. Associate Fellow AIAA.

Introduction

WIND tunnels are used to test the aerodynamic characteristics of aircraft, and the influence of the tunnel walls must be taken into account when considering test results. Historically, wind-tunnel corrections have been based on linear potential flow theory.[1] To obtain good quality and reliable test data, factors relating to wall interference, flow angularity, local variations in velocity, and support interference must be taken into account. Karou[2] found that for delta wings with aspect ratio equal to one and spanning up to half the tunnel width, classical wall correction techniques can be used to correct flowfield and force results up to 30-deg angle of attack. (Note that vortex breakdown was unlikely to be present over the wing.) Also, for swept wings with a blockage ratio (ratio of model planform area to tunnel cross-sectional area) of less than 0.08, tunnel interference effects can usually be considered negligible.[3]

Clearly, the flow conditions within a wind tunnel will be different from those a wing would experience in free air. The interactions between the wing and wall flowfields induce longitudinal and lateral variations (streamline curvature and aerodynamic twist, respectively) to the freestream, in addition to those attributed to the wing alone. These differences may result in a reduction in the average downwash experienced by the model, a change in the streamline curvature about the model, an alteration to the local angle of attack along the span of the model, and changes in dynamic pressure about the model due to solid and wake blockage and in the buoyancy effect due to the axial pressure gradient along the tunnel test section. The magnitude of these effects increases with model size (increasing solid blockage).

Weinberg[4] conducted an experimental investigation into wall effects. Two sets of three wings were tested (one set with 60-deg sweep and one set with 70-deg sweep), each wing with a different span size. The experiment was performed in a square water tunnel (low Reynolds-number) at a constant flow velocity of 11 m/s. The tunnel size was 45 × 45 cm. He found that for the three wings with 70-deg sweep, as the wing size was increased and at a constant angle of attack, vortex breakdown moved downstream. For the three wings with 60-deg sweep, he found that, as the wing span-to-tunnel width ratio increased from 0.175 to 0.35, the wall effects followed

similar trends, that is, vortex breakdown was shifted downstream with increasing wing size. However, when the wing span-to-tunnel width ratio was increased from 0.35 to 0.7, no significant change was observed. This suggested that effective camber was not the only influence. For both the 60- and the 70-deg wings, the difference in breakdown location observed from the smallest model to the largest model was of the order $25\%c_r$.

Thompson and Nelson[5] investigated experimentally the influence of tunnel walls on a 70-deg delta wing by testing full-, two-thirds-, and half-scale models in a square tunnel. (The largest model gave the ratios $b/H = b/W = 0.364$.) Because of a steady hysteresis effect, the wing was tested for a quasi-steady upward stroke and a downward stroke. It was found that for the smallest model tested ($b/H = b/W = 0.124$) the breakdown location shifted downstream by as much as $15\%c_r$ on both the quasi-steady upstroke and downstroke. For the half-scale model and the full-scale model, there appeared to be little difference in the breakdown locations. As stated by Thompson and Nelson, this shift downstream as model size is decreased is in contrast to the results of Weinberg.[4] Weinberg used a Reynolds number an order of magnitude lower, and a constant velocity, as opposed to keeping the Reynolds number constant (as in the experiments of Thompson and Nelson). The vortex suction on the model surface increased with model size.

More recently, Pelletier and Nelson[6] studied the effect of tunnel interference on 70-deg delta wings. Experiments were conducted in a water tunnel with three different sized wings. These low Reynolds number tests agreed with the previous findings of Thompson and Nelson,[5] who tested at higher Reynolds number, in that breakdown moved toward the apex with increasing wing size. Pelletier and Nelson used the method of images to explain this effect, concluding that the tunnel walls increased the mean incidence of the wing, thus, promoting breakdown.

Verhaagen et al.[7] performed Euler calculations of the flow over a 76-deg delta wing inside wind tunnels of increasing size. The wing span-to-tunnel width ratios considered were 0.292, 0.389, and 0.584, and the test section was octagonal. To model the effect of a secondary separation, a small fence was placed where secondary separation would occur. It was found that decreasing the tunnel size (increasing the wing span-to-tunnel width ratio) increased the suction in the vortices and increased the velocities in the vortex core, due to an increase in circulation with decreasing tunnel size.

Mitchell[8] tested a at upper and lower surface 70-deg delta wing at 27-deg angle of attack in the ONERA S2Ch and ONERA F2 tunnels. The tests had model span-to-tunnel width ratios of 0.23 and 0.49, respectively. It was found that the mean location of breakdown was upstream (around $7\%c_r$) in the narrower ONERA F2 tunnel in comparison to the larger ONERA S2Ch tunnel.

Allan et al.[9] performed Euler simulations of tunnel interference effects on a 65-deg delta wing in various tunnels for static and pitching cases. It was observed that tunnel side walls were the most influential factor on breakdown location with roof and floor having little effect. It was also noted that in pitching simulations the tunnel interference effects were strongest on the downstroke, during the vortex reformation.

Allan et al.[10] performed Reynolds averaged Navier–Stokes RANS simulations of a 70-deg delta wing in a wind tunnel, with and without downstream support structures. It was found that the level of support structure interference was heavily dependent on whether or not the vortex cores impinged on the support. Using tunnel centerline supports with small models may promote vortex breakdown, with breakdown moving downstream as the model size increases (as the core trajectory moves away from the centerline and interference region).

It is the aim of this work to confirm the previous Euler results and suggest best practices for tunnel testing of delta wings.

Flow Solver

All simulations described in this paper were performed using the University of Glasgow parallel multiblock (PMB) Reynolds averaged Navier–Stokes (RANS) solver. A full discussion of the code and turbulence models implemented is given in Ref. 11. PMB uses a cell-centered finite volume technique to solve the Euler and RANS equations. The diffusive terms are discretized using a central differencing scheme, and the convective terms use Roe's scheme with MUSCL interpolation offering third-order accuracy. Steady flow calculations proceed in two parts, initially running an explicit scheme to smooth out the flow solution, then switching to an implicit scheme to obtain faster convergence. The preconditioning is based on block incomplete lower–upper factorization and is also decoupled between blocks to increase the parallel performance. The linear system arising at each implicit step is solved using a generalized conjugate gradient method. For time-accurate simulations, Jameson's pseudotime (dual-time stepping) formulation[12] is applied, with the steady-state solver used to calculate the pseudosteady states at each physical time step.

The RANS equations are solved, and the two-equation k–ω turbulence model is used for closure. It is well known that most linear two-equation turbulence models overpredict the eddy viscosity within vortex cores, thus, causing too much diffusion of vorticity.[13] This weakens the strength of the vortices and can eliminate secondary vortices, especially at low angles of attack, where the vortices are already weak. The modification suggested by Brandsma et al.[14] was, therefore, applied to the standard k–ω model of Wilcox[15] to reduce the eddy viscosity in vortex cores, by limiting the production of turbulent kinetic energy k, as

$$P_k = \min\left\{P_k^u, (2.0 + 2.0\min\{0, r-1\})\rho\beta^* k\omega\right\} \qquad (1)$$

Here P_k^u is the unlimited production of k and r is the ratio of the magnitude of the rate of strain and vorticity tensors. When k is overpredicted in the vortex core, it will be limited to a value relative to the dissipation in that region. After comparison with experiment,[14,16,17] this modification was found to improve predictions compared with the standard k–ω turbulence model and is, therefore, used in all simulations presented.

The Computational Fluid Dynamics Laboratory at the University of Glasgow owns a cluster of personal computers. The cluster is known collectively as Jupiter and is fully described by Badcock et al.[18] The cluster used for this study has 32 nodes of 750-MHz AMD Athlon Thunderbird uniprocessor machines, each with 768 MB of 100-MHz dynamic random access memory (DRAM). Message passing interface (MPI) is used to link up multiple nodes to create a virtual machine, which is used to execute computationally demanding problems. PMB balances the node loadings (number of cells per node) by spreading the blocks over all of the nodes of the virtual machine. Halo cell values are passed between adjacent blocks using MPI.

Test Cases

The wing used for all work described is that of the WEAG-TA15 WB1 65-deg sweep delta wing. The WEAG-TA15 WB1 model (Fig. 1) was tested at DLR, German Aerospace Research Center, Braunschweig, Germany, by Löser.[19] Experiments were carried out at two freestream Mach numbers (0.06 and 0.12) with Reynolds numbers based on the root chord of 1.55×10^6 and 3.1×10^6. The experiments were carried out in the 2.85×3.2 m low-speed atmospheric wind tunnel (NWB) of DNW, located at DLR Braunschweig, using the open test section.

The wind-tunnel model had an inner chord of 1200 mm, a tip chord of 180 mm, and a leading edge sweep of 65 deg. The model is fully symmetric with a sharp leading edge, which has a radius of 0.25 mm. The aerofoil consists of an arc segment from the leading edge to 40% of the local chord, the region 40%–75% of the local chord is defined by the NACA 64A005 aerofoil, and from 75% of the local chord to the trailing edge the aerofoil is a straight line inclined at 3 deg. The wind-tunnel model has a fuselage of 160 mm diameter built into the lower surface of the wing, though this is not expected to influence the upper surface flow. The fuselage was not modeled in the current work.

The computational test cases in Table 1 were considered. Four boundary conditions were specified relating to free air and in-tunnel situations. The first case was that of far-field conditions specified at the outer boundaries with all boundaries being $10c_r$ from the wing.

Table 1 Summary of test cases

Tunnel	b/W	b/H	α, deg	M_∞	Re
Far field	——	——	21	0.2	3.1×10^6
3×3	0.42	0.42	21	0.2	3.1×10^6
3×2	0.42	0.63	21	0.2	3.1×10^6
2×3	0.63	0.42	21	0.2	3.1×10^6
Far field	——	——	22	0.2	3.1×10^6
Far field	——	——	23	0.2	3.1×10^6
Experiment	——	——	21	0.12	3.1×10^6

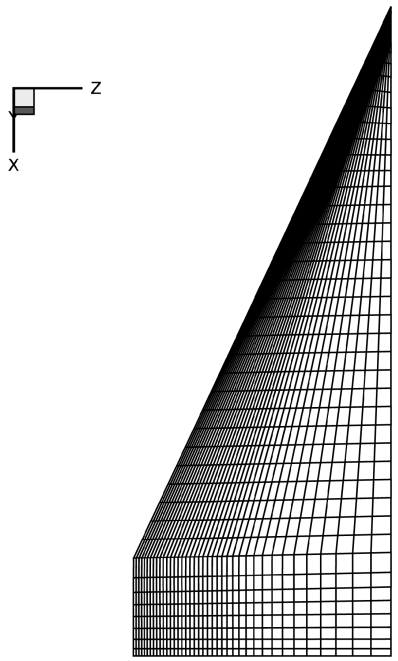

Fig. 1 WEAG-TA15 wing surface mesh (every second point removed for clarity).

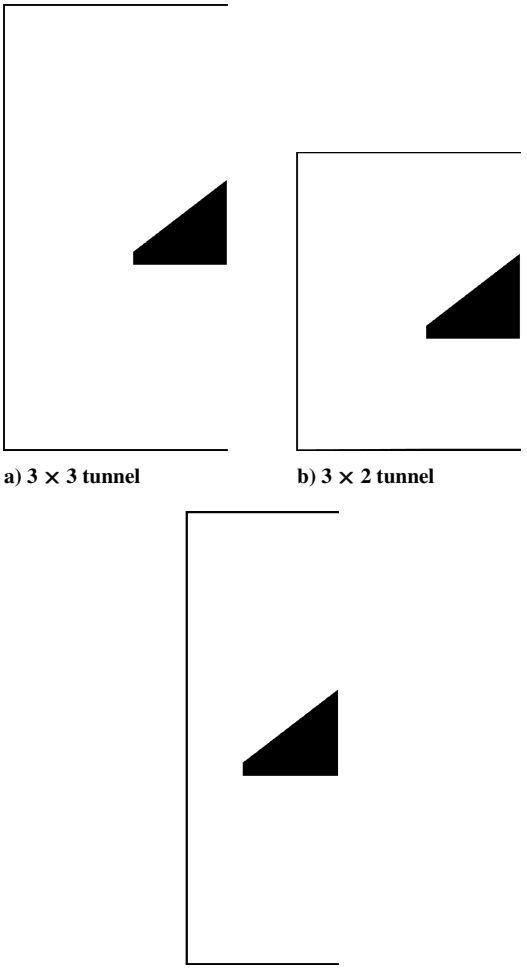

a) 3 × 3 tunnel **b) 3 × 2 tunnel**

c) 2 × 3 tunnel

Fig. 2 Wind-tunnel shapes considered in this study.

The remaining three cases represent a 3×3 (square cross section), a 3×2 (equivalent to bringing the 3×3 tunnel roof and floor closer to the wing), and a 2×3 tunnel (equivalent to bringing the 3×3 side walls closer to the wing). No tunnel contraction or diffuser were modeled because their geometries are unique to a specific tunnel. Instead far-field conditions were specified at the tunnel inlet located $10c_r$ upstream of the wing. An extrapolation boundary condition was set $10c_r$ downstream of the wing. Inviscid wall conditions were applied at the tunnel walls to avoid the grid sizes required to model the tunnel boundary layers. For all four cases mentioned, the wing is meshed inside the tunnel at 21 deg and steady fully turbulent flow is assumed. A symmetry condition along the root chord of the wing was also used, requiring only half the wing to be meshed. At the angle of attack considered in the current study, it is expected that the flow will be symmetric. Two additional cases were also considered that had far-field conditions as in the first case, with the freestream velocity vector rotated such that the wing was at an angle of attack of 22 and 23 deg.

To be able to perform a fair comparison between different tunnels, it was decided that one mesh should be constructed in such a way that removing outer blocks would allow different tunnel shapes to be assessed. This has the advantage that the resolution of the flow is constant, irrespective of tunnel shape; thus any variations are occuring due to the presence and location of walls and roof and floor. The topology that facilitated this was the H–H topology. Views of the wing in the tunnels are shown in Fig. 2. Initial cell spacing normal to the wing was $1.0 \times 10^{-6} c_r$, giving $y^+ < 1.0$ over the wing.

Sinusoidal pitching computations were at a Reynolds number of 3.1×10^6 and Mach number of 0.2, with a pitching amplitude of 6 deg and reduced frequency of motion K of 0.56. There were 50 time steps per cycle with 4 complete cycles being computed. A pitching calculation was performed with 100 time steps per cycle to ensure an adequate temporal resolution, and it was concluded that 50 time steps per cycle was sufficient.[16]

Verification and Validation

Because the experimental data of Löser[19] was obtained in an open test section wind tunnel, the far-field case at 21-deg angle of attack is used for validation of the steady and pitching solutions.

To verify the accuracy of the solutions, a grid-dependence study was conducted. Visbal and Gordnier[20] observed for a 75-deg delta wing that breakdown moved downstream with grid refinement; however, the finest grid used was of a lower density than the current standard grid. Because of computational limitations, the resolution of the grid was doubled by increasing the number of points in the direction normal to the wing only. However, it has been shown with Euler simulations (see Ref. 16) that the flow is most sensitive to refinement in this direction. Figure 3 shows the upper surface pressure distributions obtained on the square tunnel grid. As can be seen, at $x/c_r = 0.3$ and 0.6 the differences are minimal; however, at $x/c_r = 0.8$, there is a slight variation. This is likely due to a slight difference in vortex breakdown position in this region. We can, therefore, consider the solutions grid converged. In any case, because an identical resolution of the vortical region is used in all simulations, any possible grid dependency will be common to all solutions. As will be discussed, the trends are also identical with Euler and RANS models of the flow.

A comparison of the computed and experimental surface pressures at three chordwise locations is given in Fig. 4. As can be seen, the primary vortex suction levels compare very well with experiment at the chordwise locations of $x/c_r = 0.3$, $x/c_r = 0.6$, and $x/c_r = 0.8$.

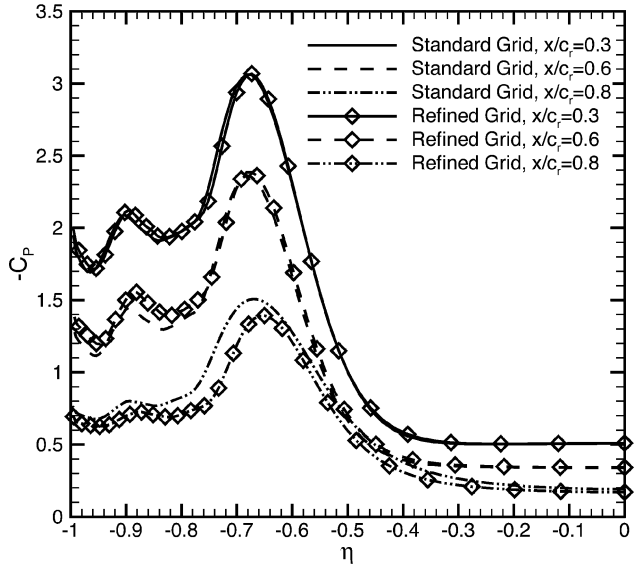

Fig. 3 Grid refinement study; upper surface pressure distributions, square tunnel.

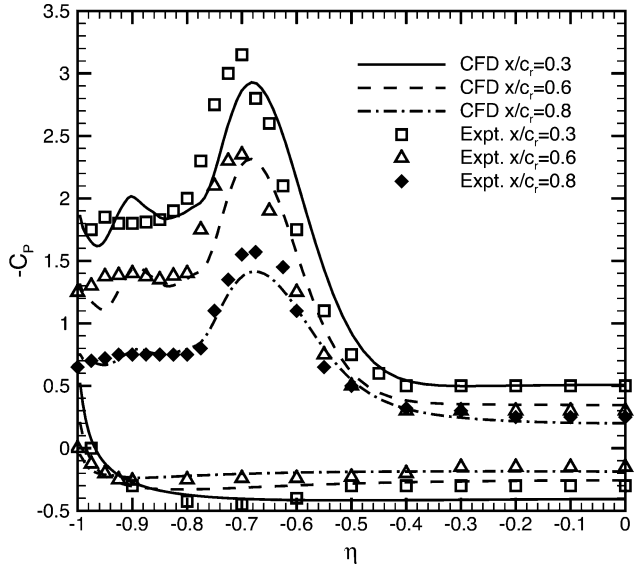

Fig. 4 Comparison of computed upper surface pressure distributions with experiment.

However, one noticeable difference is the location of the primary vortex core. In the CFD solution, the primary vortex core is clearly more inboard than was observed in the experiment (most evident at the chordwise locations of $x/c_r = 0.3$ and 0.6). This indicates that the secondary vortex is too large because a larger secondary vortex will push the primary vortex core inboard and away from the surface. (The secondary separation occurs too early, which is likely due to turbulence model predictions of the boundary-layer profile.) This is the reason for the slightly lower primary suction peaks predicted in comparison to experiment. Further evidence of the large secondary vortex is that the secondary suction region predicted by CFD is more "peaked" (most evident at the chordwise locations of $x/c_r = 0.3$ and 0.6) than that found in experiment. The early secondary separation can be attributed to the turbulence levels in the boundary layer predicted by the modified k–ω model. (Low levels of turbulence in the boundary layer will cause early secondary separation.) Interestingly, at the chordwise location of $x/c_r = 0.8$, the primary and secondary suction levels compare very well with experiment, and as such, the primary vortex core location is also well predicted. Note that at this chordwise location there is a smaller spanwise pressure gradient (due to the vortices being burst), thus, reducing the dependency of the solution on the boundary-layer profile. Despite the more inboard primary vortex in the CFD solutions, it is concluded that the leeward flow over the WEAG-TA15 wing has been well predicted.

All steady simulations described in this paper were converged at least six orders of magnitude.

Results and Discussion

Steady Results

Before pitching simulations were conducted, the steady cases were considered. The breakdown locations for all steady test cases are given in Table 2. Note that no experimental breakdown locations were available.

The breakdown locations were obtained by extracting a vertical slice through the vortex core and locating the point where the chordwise velocity component becomes negative. It can be seen that the trend of breakdown location with tunnel wall constraints predicted by the RANS solver are similar to those predicted by the Euler equations (see Ref. 9). For the 3×3 and 3×2 tunnels, it can be seen that the breakdown locations are almost identical nearer the apex in comparison to the far-field results. This indicates that the roof and floor proximity has little influence. Comparing the 2×3 tunnel breakdown locations with those from the 3×3 and 3×2 tunnels, we clearly see that the largest influence on breakdown location is the side wall proximity. This agrees qualitatively with the Euler results of Allan et al.[9] To give an indication of how the mean angle of attack of the wing has varied in the tunnels, we see that the 3×3 and 3×2 tunnel breakdown locations are similar to those of the wing in free air at 22-deg angle of attack, and the 2×3 tunnel breakdown location is similar to that of the wing in free air at 23-deg angle of attack.

A comparison of the upper surface pressure distributions at two chordwise locations are given in Figs. 5 and 6. As with Euler simulations (see Ref. 9), it is clear that for the wing in a tunnel the suction peak beneath the primary vortex core increases (by up to

Table 2 Summary of steady breakdown locations for WEAG-TA15 wing

Tunnel	α, deg	b/W	b/H	Breakdown location, $\%c_r$
Far field	21	——	——	81
3×3	21	0.42	0.42	77
3×2	21	0.42	0.63	77
2×3	21	0.63	0.42	71
Far field	22	——	——	77
Far field	23	——	——	71

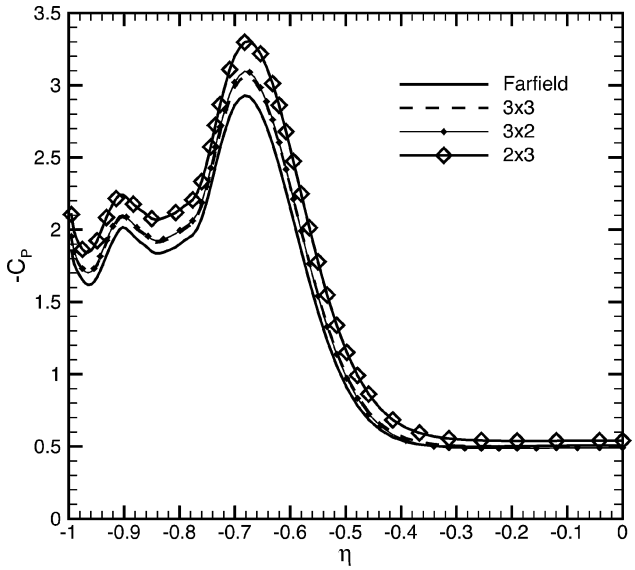

Fig. 5 Comparison of upper surface pressure distributions, $x/c_r = 0.3$.

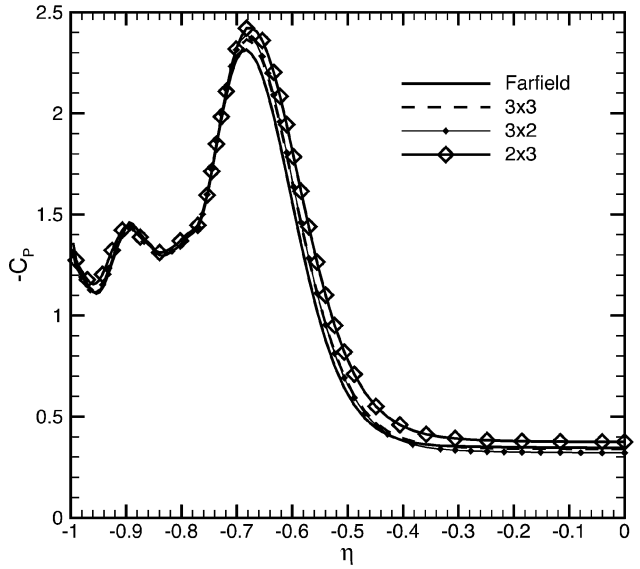

Fig. 6 Comparison of upper surface pressure distributions, $x/c_r = 0.6$.

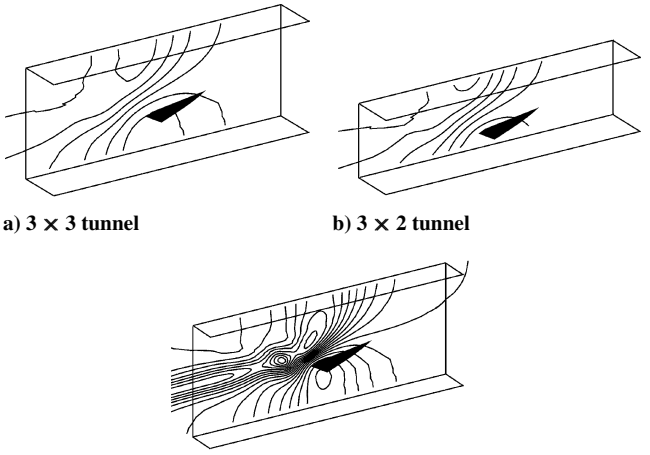

a) 3 × 3 tunnel **b) 3 × 2 tunnel**

c) 2 × 3 tunnel

Fig. 7 Tunnel wall pressure distributions.

13% in the 2 × 3 tunnel at 30%c_r). Although not presented here, it has been seen that there is a minor shift in the secondary separation location toward the leading edge of the wing, when the wing is placed in a tunnel.[16] Any delay in secondary separation is likely to be dependent on the upper surface shape, the primary suction peak, and the crossow momentum. (Note that the WEAG-TA15 wing has a convex upper surface.) A more apparent shift in secondary separation location was observed in tunnel interference effects on a flat upper surface 70-deg delta wing.[10] Inboard of the primary vortices (near the wing root), it can be seen that there is additional suction (about 10–15% in the 2 × 3 tunnel) on the wing upper surface due to the blockage effect of the tunnels. It is also evident that when the roof and floor are brought closer to the wing there is little change in the suction peak (compare the 3 × 2 and 3 × 3 tunnel solutions), which indicates that roof and floor proximity has little bearing on the strength of the vortices.

The tunnel wall pressure distributions for all three tunnels are given in Fig. 7. As in the Euler solutions (see Ref. 9), there is a clear favorable pressure gradient in the axial direction. This is expected because the vortices become closer to the side wall as they extend toward the trailing edge of the wing. At the cropped tip of the wing, the side wall induced upwash will be greatest, producing the largest suction on the wall. Looking at the strength of the pressure contours, the pressure gradient on the wall becomes more favorable as the side wall is moved closer to the wing, which is seen as we move from the 3 × 3 to the 2 × 3 tunnel. Again, as seen in Euler solutions, there is a clear vortical flow pattern on the side wall downstream of the wing's trailing edge. This vortical flow pattern extends the length of the tunnel. The vortical flow pattern on the side walls is observed for the three tunnels, reducing in extent with decreasing b/W ratio.[21] It is clear that the close proximity of the 2 × 3 tunnel side wall induces the largest favorable pressure gradient, which indicates that the side wall produces the most detrimental interference.

To assess the adverse pressure gradient experienced by the vortex core in the tunnels, the pressure distribution along the leading-edge vortex core is shown in Fig. 8. As the vortex is placed within tunnel constraints, it can be seen that the suction in the vortex core increases, with the largest increment being observed in the 2 × 3 tunnel, where the maximum suction is around 15% greater than that for the far-field solution. The 3 × 3 and 3 × 2 tunnels produce a similar increment in suction (of around 6% in comparison to that of the far-field solution). This increase induces a stronger adverse pressure gradient, as seen in Fig. 8, thus, promoting vortex breakdown.

The flow angles (the angle at which the flow is deflected due to the presence of the wing) at the 2 × 3 tunnel side wall location are shown in Fig. 9. As in the Euler results (see Ref. 9), it can be seen that the presence of the side walls has increased the flow angles along the wing, thus, increasing the mean effective incidence of the

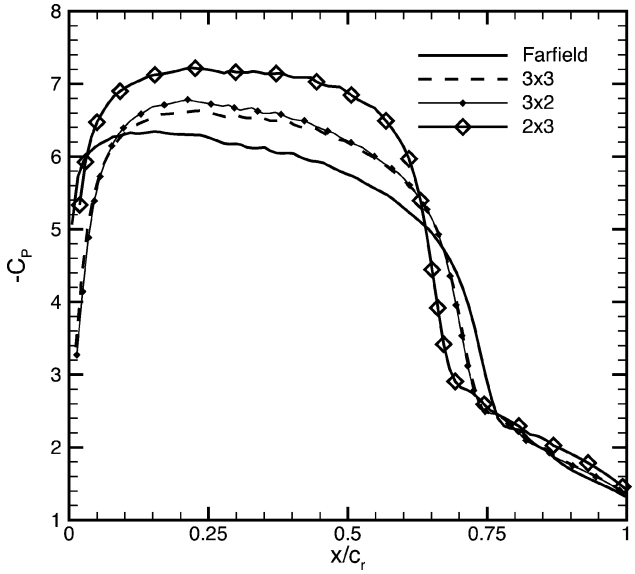

Fig. 8 Pressure distributions along vortex core.

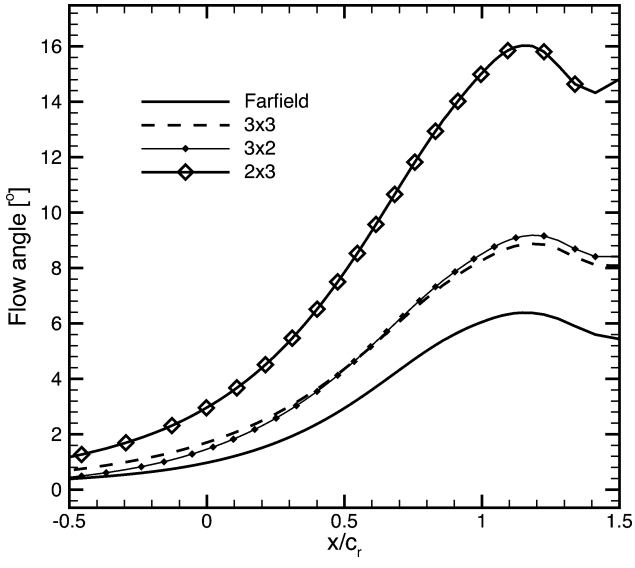

Fig. 9 Flow angles at 2 × 3 tunnel side wall location.

wing. Evidently the proximity of the 2×3 tunnel side wall induces the largest mean incidence, followed by the 3×3 and 3×2 tunnels, which induce a near equal mean incidence. Clearly it is the presence of the side wall that will influence how much the mean effective incidence changes. Because the breakdown location moves upstream, it would appear that the increase in mean effective incidence is dominant over the induced camber effect.

The helix angle of the flow through the vortex core can be seen in Fig. 10. These data were extracted at a chordwise location of $60\%c_r$, where breakdown is downstream in all solutions. The helix angle increases due to the side wall-induced velocity components, and clearly the roof and floor again have little effect. The vortex tightens the most in the 2×3 tunnel, followed by the 3×3 and 3×2 tunnels, which are nearly equal. An increase in helix angle is well known to promote vortex breakdown.[22]

The tunnel centerline pressure distributions can be seen in Fig. 11. It can be seen that the 3×2 and 2×3 tunnels produce similar blockage levels ahead of the wing. The jump from the pressure side to the suction side of the wing can be seen around $x/c_r = 0.5625$. As already observed, when the wing is placed within wind tunnels the static pressure increases on the lower surface and decreases on the upper surface (due to the blockage effect). As in Euler solutions (see Ref. 9), well downstream of the wing the pressure distributions

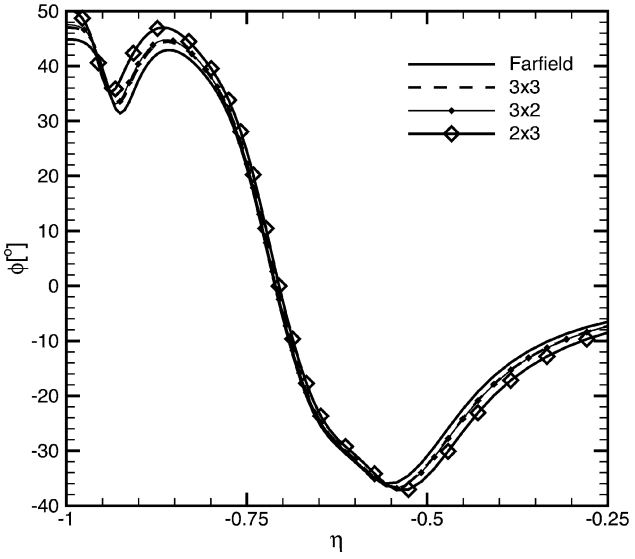

Fig. 10 Comparison of helix angles, $x/c_r = 0.6$.

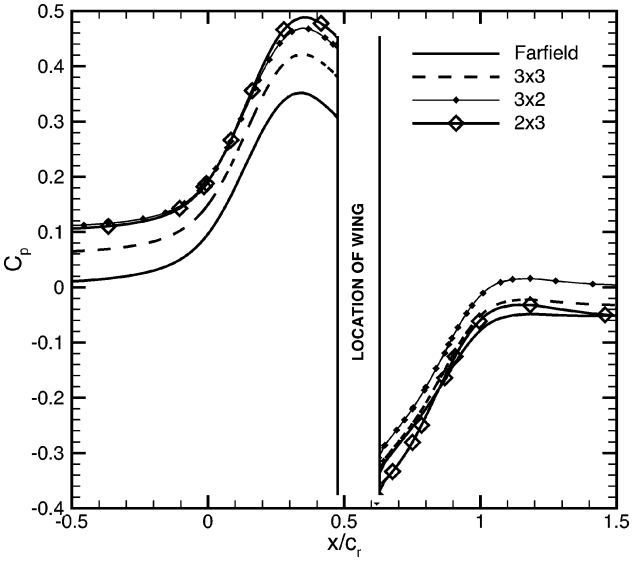

Fig. 11 Tunnel centerline pressure distributions.

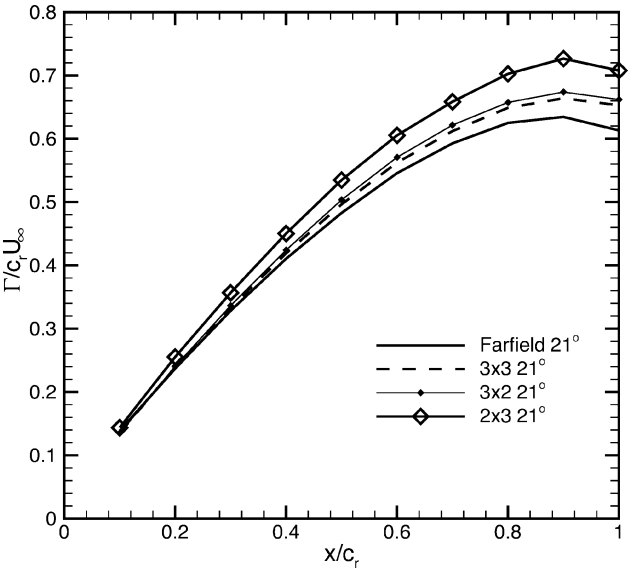

Fig. 12 Comparison of circulation distributions.

indicate that the broken down vortical system is displaced upward into the center of the tunnel. In the vicinity of the broken down swirling flow, there will be a reduction in pressure relative to the static pressure in the tunnel. Thus, near the trailing edge, where the flow on the lower surface is expanding, the 2×3 tunnel solution exhibits characteristics of the vortical flow being displaced to the centerline of the tunnel. Despite the pressure near the trailing edge being higher in the 2×3 tunnel than in the far-field solution, one must recall the increment in pressure due to blockage. Thus, when the effect of blockage is deducted, it is clear the flow past the trailing edge must be lifted in the 2×3 tunnel in comparison to the far-field, 3×3, and 3×2 tunnel solutions (because there is a reduction in static pressure due to the presence of the displaced broken down swirling flow). This was confirmed via flow visualization.

The chordwise distributions of circulation for the 21-deg cases are given in Fig. 12. The circulation was computed by integrating the axial component of vorticity over entire chordwise slices through the domain. The secondary vortex was eliminated from the calculation of circulation because the axial vorticity component of the secondary vortex is of opposite sign to that of the primary vortex. Clearly the tunnel walls increase the strength of the vortices in the chordwise direction, with the 2×3 side wall inducing the strongest vortices (increasing the circulation by up to 15% near the trailing edge in the 2×3 tunnel). The almost equal circulation near the apex, and the steeper gradient of the circulation curve in the tunnels, indicates that the effect of the tunnel side walls increases down the leading edge as expected. Because the 3×3 and 3×2 tunnels produce similar strength vortices, the roof and floor have little influence on vortex strength.

We now compare the effect of the 2×3 tunnel walls with the effect of increased mean incidence in Fig. 13. Here we see that increasing the mean incidence of the wing has the effect of shifting the curves upward, with slightly increasing gradient. This is in contrast to the effect of the side walls. If we compare the 2×3 tunnel curve with that of the far-field solutions, we see that near the apex the vortex strength is close to the 21-deg case, becoming stronger than the 23-deg case near the trailing edge. This is due to the induced camber effect. Such a result may have important implications for correcting parameters such as pitching moment. Despite vortex breakdown being at a similar location in the 2×3 tunnel compared with that of the wing in free air at 23-deg angle of attack, the variation in circulation along the length of the vortex is quite different.

Pitching Results

The lift, drag, and pitching moment curves from each of the pitching cases considered are compared with the experimentally obtained

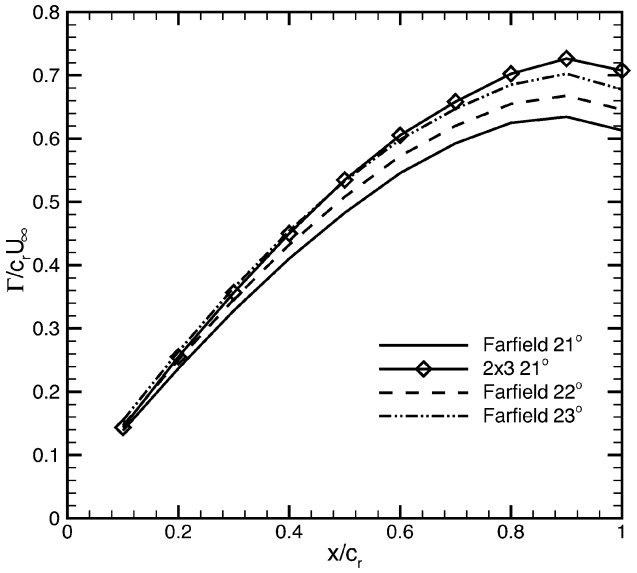

Fig. 13 Comparison of circulation distributions.

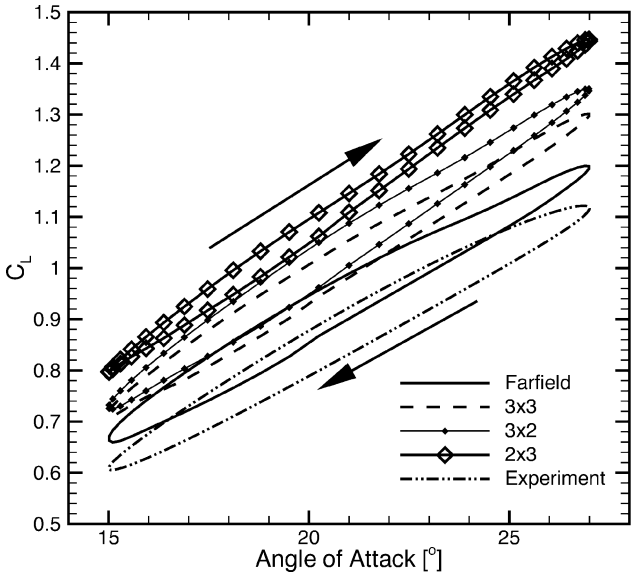

Fig. 14 WEAG-TA15 wing, C_L–α curves for pitching motion.

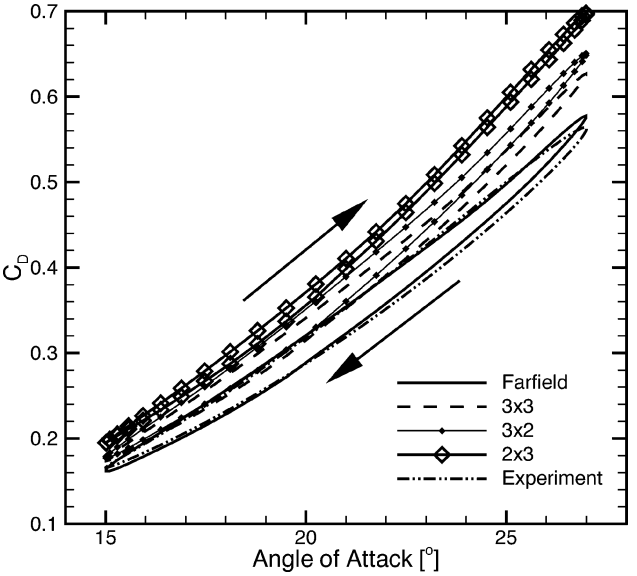

Fig. 15 WEAG-TA15 wing, C_D–α curves for pitching motion.

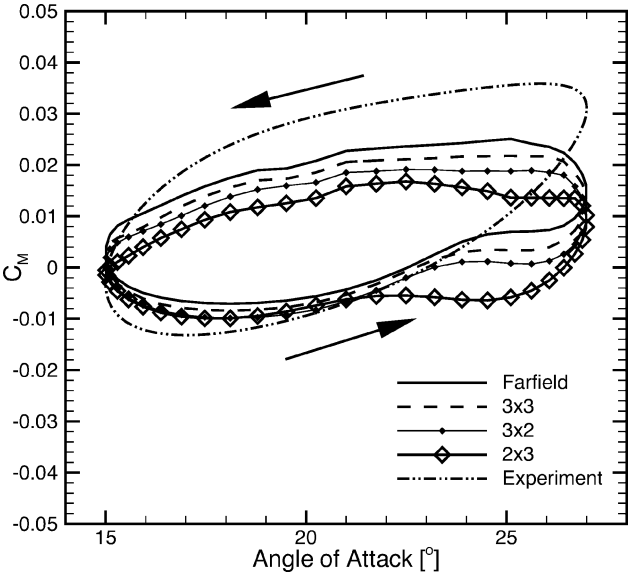

Fig. 16 WEAG-TA15 wing, C_M–α curves for pitching motion.

loads and moments in Figs. 14–16. The pitching motion of the wing is defined by the sinusoidal function given by Eq. (2). The reduced frequency K of the pitching motion was 0.56, with the mean incidence α_m being 21 deg and the amplitude α_0, being 6 deg. Thus,

$$\alpha(\tau) = \alpha_m + \alpha_0 \sin(K\tau) \tag{2}$$

For validation purposes, the far-field solution is considered. The lift and drag curves can be seen to have been predicted well, with the lift being slightly overpredicted. The magnitude of the pitching moment curves has also been predicted well, though the trend is not so well predicted. However, note that parameters such as pitching moment are very sensitive to vortex breakdown location and vortex strength, which are hard to predict to a high level of accuracy with current RANS methods. As can be seen, particularly in the lift curve, there is a thinning of the hysteresis loop as the angle of attack is increased. This is due to a region of reduced lift curve slope occurring at around 23-deg angle of attack. At this incidence it is observed from flow visualizations that vortex breakdown has crossed the trailing edge, resulting in a reduction in the lift curve slope.[23] The resulting nonlinearity is not observed in the experimental data, which may be a result of the data presentation. [The experimental data are given in the frequency domain via Fourier transformation (see Ref. 19).] The response of the vortices to pitching motion is predicted sufficiently well, and as such, comparisons of vortex response to pitching motion in tunnels can be considered.

Considering first the lift and drag curves in Figs. 14 and 15, we initially see that the tunnels have a considerable influence on the shape and positions of the curves. As the wing is placed into the 3×3 tunnel, we see an increment of the lift curve. There is also a narrowing of the curve, most evident at the higher incidence. This can be attributed to the vortex breakdown passing the trailing edge at a slightly lower angle of attack when compared with the far-field solution. A similar situation is seen in the 3×2 tunnel where the curve is further incremented due to increasing blockage effects. As expected, the location at which the lift curve slope drops (when breakdown crosses the trailing edge) appears to be similar in the 3×3 and 3×2 tunnels. Finally, comparing the 2×3 tunnel solution with that from the far-field solution, we see a further increment in lift as expected with the stronger vortices. Also it is evident that by far the thinnest loops occur for the 2×3 tunnel solution. Again, this is because vortex breakdown has crossed the trailing edge earliest in the 2×3 tunnel. A similar situation is seen with the drag curves. The thinning of the hysteresis loops can be explained as follows. Because

the effect of increasing blockage is to increment the lift and drag, the vortex lift contribution (recalling Polhamus's suction analogy[24]) becomes a lower percentage of the total lift. Therefore, when the blockage is increased and the potential lift component becomes larger, the hysteresis due to vortex lift contribution becomes less apparent. If we compare against Euler solutions (see Ref. 9), where the vortices are closer to the surface and, therefore, the vortex lift is higher, the effect of the increase in potential lift on the hysteresis loop width is lower. Also because the vortices are closer to the wing in the Euler solutions, an increase in vortex strength, that is, as incidence or b/W ratio increases, will be more apparent on the suction peaks (and, therefore, the vortex lift) in comparison to the RANS solutions.

The pitching moment curves provide a good measure of how much the flow structure varies at a given point in the pitching cycle due to tunnel wall constraints. Because breakdown locations are unavailable once breakdown has passed the trailing edge (due to the grid density decreasing in that region), the pitching moment curves provide a great deal of insight as to how the tunnel walls are influencing the flow at the low incidences, being sensitive to longitudinal flow variations. The understanding of the side wall influences on breakdown location gained from the steady results, and the effect that blockage has on the loads and moments, allows a great deal of information to be interpreted solely from the pitching moment curves. Figure 16 shows the pitching moment curves obtained from each solution. Clearly the smallest difference is in the angle of attack range 15–21 deg on the upstroke of the pitching motion. When it is recalled that the blockage in the 2×3 and 3×2 tunnels is similar (which will have an effect on the pitching moment), it can be concluded that, because the pitching moment curves in the 2×3 and 3×2 tunnels are almost identical in the low incidence range, the tunnel side walls have a lesser influence on the vortices. Also note that wind-tunnel wall interference will depend heavily on vortex strength, which increases with incidence. (The mirror images strengthen as the leading edge vortices strengthen.) Thus, we would expect the greatest interference to occur at high incidence. It can, therefore, be assumed that, at low incidence, the difference between the 2×3 and 3×2 tunnel curves, and those from the 3×3 and far-field solutions, is purely due to blockage.

As the incidence is increased and the influence of the tunnel side walls increases, the effect of the promotion of vortex breakdown crossing the trailing edge early in the 2×3 tunnel can be seen at around 22 deg on the upstroke. Because the breakdown forms just past the trailing edge, there is a slight increase in the nose down pitching moment due to the breakdown region acting like a bluff body in the CFD solutions. (A small suction peak is observed on the wing surface beneath the vortex breakdown region.) This provides additional suction near the trailing edge, increasing the nose down pitching moment slightly. As the incidence increases further and breakdown moves completely onto the wing, a loss of the nose down pitching moment occurs as expected. (This occurs earliest in the 2×3 tunnel at around 24.5 deg.) The solutions from the other two tunnels and the far-field solution follow a similar pattern, although this occurs later in the pitching cycle. At around 25 deg, it is evident that vortex breakdown is well established over the wing in all of the solutions (Fig. 17), which is highlighted by a sharp decrease in the nose down pitching moment.

Now consider only the 2×3 tunnel pitching moment curve: It can be seen that from 27 deg to around 25 deg on the downstroke that the pitching moment remains relatively constant. In this region, vortex breakdown is held at its most upstream location (Fig. 17 for confirmation) due to the increased influence of the tunnel walls at high incidence, which are promoting vortex breakdown. It can be concluded that, as in Euler simulations (see Ref. 9), there is a delay in vortex recovery. From around 25 to 22 deg, it is observed that the 2×3 tunnel solution tends toward that of the other tunnels, due to the reducing tunnel interference. From around 22 deg downward, it can be seen that the pitching moment curves from all tunnels follow a similar trend to that of the far-field solution as the tunnel interference decreases. Most attention has been paid to the 2×3 tunnel solution: however, it is also clear that the 3×3 and 3×2 tunnels have influenced the curves, both in blockage terms and from a slight promotion of vortex breakdown.

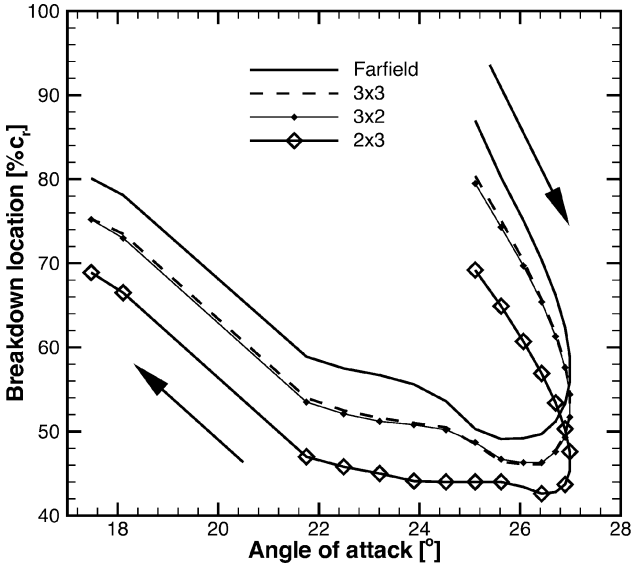

Fig. 17 WEAG-TA15 wing, unsteady breakdown locations for sinusoidal pitching motion.

The vortex breakdown locations for the RANS pitching calculations are given in Fig. 17. Only locations at which breakdown is over the wing are shown. Downstream of the trailing edge, the grid coarsens, and as such, breakdown locations cannot be obtained in this region. Note that on the upstroke the vortex breakdown location has been taken where the axial component of velocity becomes zero. However, on the downstroke of the motion where vortex breakdown is moving downstream, it is not possible to use this criterion for breakdown because the motion of the breakdown location prohibits this. (The axial velocity does not become zero.) As such, for the downstroke the breakdown location was defined as the location where the turbulent Reynolds number (or equally the eddy viscosity) increases rapidly. A turbulence Reynolds number of near 600.0 (where eddy viscosity is 600 times greater than the molecular viscosity) was chosen as the breakdown location, which corresponded well with where the axial velocity was observed to become zero on the upstroke. As the wing pitches up, the breakdown clearly moves upstream in a near linear manner, reaching its most upstream value at around 26 deg on the downstroke. In the 2×3 tunnel, in particular, it can be seen that the breakdown is held near its most upstream location until around 24 deg on the downstroke. This is because the tendency of the side walls is to promote vortex breakdown; thus, at the high incidence, the effect of the side walls is strong and, therefore, breakdown is held upstream. When the remainder of the downstroke is considered, as the wing pitches down it can be seen from the pitching moment curves that there is still a wide variation in pitching moment between the various solutions. This indicates that the tunnel effects are large on the downstroke of the motion because breakdown will remain over the wing for longer as the wing leaves a state of high tunnel interference. A similar trend was observed with Euler simulations (see Ref. 9).

To visualize the extent of the interference with incidence, the tunnel wall pressure distributions for the 2×3 tunnel are given in Fig. 18. The side wall interference is clearest in the solutions from the 2×3 tunnel, although the discussion applies to the other tunnels. As the wing pitches up and the vortices become stronger, we see a much stronger interference pattern on the side walls. It is this strong interference at high incidence that causes the delay in vortex recovery in the 2×3 tunnel. The effect of blockage can also be seen as a high pressure beneath the wing, increasing with frontal area blockage and incidence.

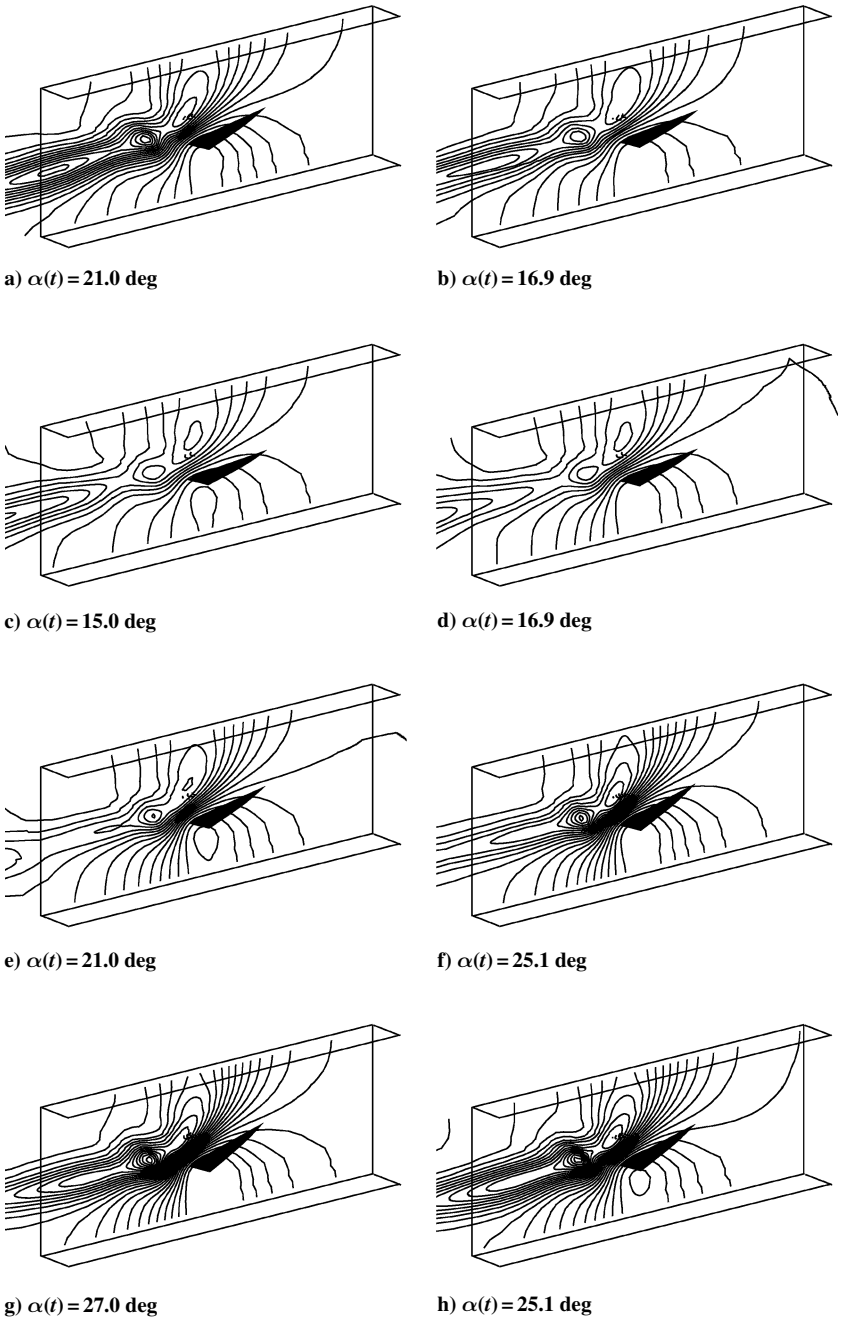

a) $\alpha(t) = 21.0$ deg b) $\alpha(t) = 16.9$ deg

c) $\alpha(t) = 15.0$ deg d) $\alpha(t) = 16.9$ deg

e) $\alpha(t) = 21.0$ deg f) $\alpha(t) = 25.1$ deg

g) $\alpha(t) = 27.0$ deg h) $\alpha(t) = 25.1$ deg

Fig. 18 Tunnel wall surface pressures during sinusoidal pitching.

Conclusions

A study has been conducted to investigate the various effects wind tunnel wall constraints have on delta wing aerodynamics. The following conclusions can be drawn from the study:

1) The simulations have confirmed that the RANS equations can adequately model the leeward surface flow over delta wings.

2) The current simulations have shown that the side walls have the dominant role in wind-tunnel interference on delta wings. Thus, models should be orientated such the side walls are a far away as possible.

3) The simulations have shown that the presence of the roof and floor has a lesser influence on vortex breakdown than that of side walls.

4) Side wall proximity consistently promotes vortex breakdown.

5) The distribution of vorticity throughout a vortex differs in tunnels when compared with free air cases. As such parameters such as pitching moment may be diffcult to correct by simply assuming a change in mean effective incidence.

6) For sinusoidal pitching motion, the extent of the breakdown variation is dependent on the wing's position in the pitching cycle.

7) Side walls have a strong influence on the rate of vortex breakdown motion, being strongest during the downstroke (vortex recovery) and weaker on the upstroke. (Breakdown travel toward the apex.)

8) The results of the current work indicate that the trends of tunnel interference predicted by RANS simulations are identical to those predicted with Euler simulations.

Acknowledgment

This work was sponsored a by QinetiQ or formerly Defence Evaluation and Research Agency (DERA) Bedford studentship.

References

[1]Garner, H. C., and Rogers, E. W. E., "Subsonic Wind Tunnel Wall Corrections," AGAR-Dograph 109, Oct. 1966.

[2]Karou, A., "Separated Vortex Flow over Slender Wings Between Side Walls–Theoretical and Experimental Investigation," Dept. of Aerospace Engineering, Rept. LR-300, Delft Univ. of Technology, Delft, The Netherlands, Aug. 1980.

[3]"Blockage Corrections for Bluff Bodies in Confined Flows," Item 80024, Engineering Sciences Data Unit, London, 1980.

[4]Weinberg, Z., "Effect of Tunnel Walls on Vortex Breakdown Location over Delta Wings," *AIAA Journal*, Vol. 30, No. 6, 1992, pp. 1584–1586.

[5]Thompson, S. A., and Nelson, R. C., "Wind Tunnel Blockage Effects on Slender Wings Undergoing Large Amplitude Motions," AIAA Paper 92-3926, July 1992.

[6]Pelletier, A., and Nelson, R. C., "Factors Influencing Vortex Breakdown over 70° Delta Wings," AIAA Paper 95-3469-CP, 1995.

[7]Verhaagen, N. G., Houtman, E. M., and Verhelst, J. M., "A Study of Wall Effect on the Flow over a Delta Wing," AIAA Paper 96-2389, 1996.

[8]Mitchell, A. M., "Caractérisation et contrôle de l'éclatement tourbillonnaire sure une aile delta aux hautes incidences," Ph.D. Dissertation, Univ. of Paris 6, Paris, July 2000.

[9]Allan, M. R., Badcock, K. J., and Richards, B. E., "A CFD Investigation of Wind Tunnel Wall Influences on Pitching Delta Wings," AIAA Paper 2002-2938, June 2002.

[10]Allan, M. R., Badcock, K. J., Barakos, G. N., and Richards, B. E., "Wind Tunnel Interference Effects on a 70° Delta Wing," Proceedings of CEAS Aerospace Aerodynamics Conference, Royal Aeronautical Society, London, 10–12 June 2003.

[11]Badcock, K. J., Woodgate, M., Stevenson, K., Richards, B. E., Allan, M., Goura, G. S. L., and Menzies, R., "Aerodynamics Studies on a Beowulf Cluster," *Parallel Computational Fluid Dynamics Practices and Theory*, edited by P. Wilders, A. Ecer, Jr., J. Periavx, N. Datofuka, and P. Fox, Elsevier Science, Amsterdam, 2002, pp. 39–46.

[12]Jameson, A., "Time Dependent Calculations Using Multigrid with Application to Unsteady Flows Past Airfoils and Wings," AIAA Paper 91-1596, June 1991.

[13]Gordnier, R. E., "Computational Study of a Turbulent Delta-Wing Flowfield Using Two-Equation Turbulence Models," AIAA Paper 96-2076, 1996.

[14]Brandsma, F. J., Kok, J. C., Dol, H. S., and Elsenaar, A., "Leading Edge Vortex Flow Computations and Comparison with DNW-HST Wind Tunnel Data," *Proceedings of the RTO/AVT Vortex Flow Symposium*, Leon, Norway, 7–11 May 2001.

[15]Wilcox, D. C., *Turbulence Modeling for CFD*, DCW Industries, La Cañada, CA, 1993.

[16]Allan, M., "A CFD Investigation of Wind Tunnel Interference on Delta Wing Aerodynamics," Ph.D. Dissertation, Univ. of Glasgow, Glasgow, Scotland, U.K., Oct. 2002.

[17]Soemarwoto, B., Boelens, O., Fritz, W., Allan, M., Ceresola, N., and Buetefisch, K., "Towards the Simulation of Unsteady Maneuvers Dominated by Vortical Flow," AIAA Paper 2003-3528, June 2003.

[18]Badcock, K. J., Richards, B. E., and Woodgate, M. A., "Elements of Computational Fluid Dynamics on Block Structured Grids Using Implicit Solvers," *Progress in Aerospace Sciences*, Vol. 36, 2000, pp. 351–392.

[19]Löser, T., "Dynamic Force and Pressure Measurements on an Oscillating Delta Wing at Low Speeds," Rept. IB 129-96/9, DLR, German Aerospace Research Center, Braunschweig, Germany, March 1996.

[20]Visbal, M. R., and Gordnier, R. E., "Compressibility Effects on Vortex Breakdown Onset Above a 75-Degree Sweep Delta Wing," *Journal of Aircraft*, Vol. 32, No. 5, 1995, pp. 936–942.

[21]Hsing, C.-C. A., and Lan, C. E., "Low-Speed Wall Interference Assessment/Correction with Vortex Flow Effect," *Journal of Aircraft*, Vol. 34, No. 2, 1997, pp. 220–227.

[22]Sarpkaya, T., "On Stationary and Travelling Vortex Breakdowns," *Journal of Fluid Mechanics*, Vol. 45, No. 3, 1971, pp. 545–559.

[23]Hummel, D., and Srinivasan, P. S., "Vortex Breakdown Effects on the Low-Speed Aerodynamic Characteristics of Slender Delta Wings in Symmetrical Flow," Journal of the Royal Aeronautical Society, Vol. 71, April 1967, pp. 319–322.

[24]Polhamus, E., "Predictions of Vortex-Lift Characteristics by a Leading-Edge Suction Analogy," *Journal of Aircraft*, Vol. 8, No. 4, 1971, pp. 193–199.